JOURNAL OF AIRCRAFT
Vol. 46, No. 4, July–August 2009

Detached-Eddy Simulation of a Wing Tip Vortex at Dynamic Stall Conditions

Kaveh Mohamed* and Siva Nadarajah†
McGill University, Montreal, Quebec H3A 2K6, Canada
and
Marius Paraschivoiu‡
Concordia University, Montreal, Quebec H3G 1M8, Canada

DOI: 10.2514/1.40685

The behavior of the tip vortex behind a square NACA0015 wing was numerically investigated. The problems studied include the stationary and the oscillating wings at static and dynamic stall conditions. Reynolds-averaged Navier–Stokes and detached-eddy simulation schemes were implemented. Vortex structures predicted by Reynolds-averaged Navier–Stokes were mainly diffused while detached-eddy simulation was able to produce qualitatively and quantitatively better results as compared to the experimental data. The breakup of the tip vortex, which started at the end of the upstroke and continued to the middle of the downstroke over an oscillation cycle, was observed in detached-eddy simulation data.

Nomenclature

C_{DES}	=	DES constant
C_s	=	Smagorinsky model constant
C_I	=	control volume I
c	=	chord length
c_p	=	constant pressure specific heat
d	=	distance from the wall
$\tilde{d}$	=	modified distance for DES
E	=	total internal energy
$E(k)$	=	3-D turbulence energy spectra
e	=	internal energy
$\mathbf{F}$	=	convective flux vectors
$\mathbf{G}$	=	viscous flux vectors
H	=	total enthalpy
k	=	thermal conductivity
$\mathbf{k}$	=	wave number
$\mathbf{P}$	=	low-speed preconditioning matrix
Pr	=	Prandtl number
p	=	pressure
r_c	=	vortex core radius
S	=	flow strain tensor
$\hat{S}$	=	entropy
t	=	time
$\mathbf{U}$	=	vector of conservative variables
$U_{i,j}$	=	velocity gradient tensor
U_∞	=	freestream velocity
u, v, w	=	Cartesian velocity components
v_θ	=	tangential velocity
$\mathbf{W}$	=	vector of entropy variables
α	=	angle of attack
Δ	=	grid spacing
ζ	=	vorticity
λ_2	=	second eigenvalue of the strain tensor
μ	=	dynamic viscosity
ν	=	kinematic viscosity
$\tilde{\nu}$	=	SA modeled viscosity
ρ	=	fluid density
σ	=	flux blending function
τ	=	shear stress
Φ_h	=	subspace of linear shape functions
ϕ_I	=	linear shape function at node I
Ω	=	computational domain
ω	=	angular velocity

Subscripts

c	=	conservative variable
d	=	pitch down
e	=	entropy variable
h	=	discretized quantity
I	=	value corresponding to node I
ss	=	static stall
t	=	turbulent variable
u	=	pitch up
x, y, z	=	directions in Cartesian system

Superscript

T	=	transpose

Received 29 August 2008; revision received 24 October 2008; accepted for publication 2 November 2008.

*Research Assistant, Mechanical Engineering Department.
†Assistant Professor, Mechanical Engineering Department. Member AIAA.
‡Associate Professor, Mechanical and Industrial Engineering Department. Member AIAA.

I. Introduction

REYNOLDS-AVERAGED Navier–Stokes (RANS) equations coupled with turbulence models have been widely denounced for their poor performance to simulate separated flows. Yet another deficiency of the RANS methodology might arise while simulating main vortical flow features away from the wall, such as the downstream evolution of a wing tip vortex. The Spalart–Allmaras (SA) turbulence model, for instance, will generate excessive turbulent viscosity along the vortex axis downstream of the wing because the existing flow vorticity keeps the production term strong while the destruction term vanishes away from the wall. Consequently, the resolution of the downstream tip vortex will be impaired due to the extreme dissipation.

With the recent increase in affordable computing power, the large-eddy simulation (LES) method has gained popularity mainly because

of producing high-fidelity flow simulation results in the separated regions. Meanwhile, the extremely fine mesh required to resolve the attached boundary-layer regions hinders the use of LES in engineering and practical applications. As practical alternatives, hybrid RANS/LES methods have been developed to exploit advantageous qualities of RANS and LES in different targeted regions of the flowfield. In particular, the detached-eddy simulation (DES) method uses the RANS approach in attached boundary layers and the LES mode in separated flows. Since its first formulation based on the SA model [1], DES has been validated on various geometries and flow conditions including circular or square cylinder [2], delta wing [3], airplane configuration [4], and the turbulent wake [5]. New formulations have been introduced to include other turbulence models such as k–ω SST (shear stress transport) [6] and LL (Lien and Leschziner) k–ε [7], and modifications have been made to improve the performance of the model at ambiguous grid spacing and low Reynolds numbers [8]. As a result, DES has become one of the primary candidates for simulating massively separated flows.

In particular, DES can be considered as an appropriate simulation tool to investigate the behavior of the tip vortex behind a wing under deep-stall oscillations. This problem requires the accurate prediction of two major flow features: the onset of the dynamic stall (DS) and the downstream evolution of the tip vortex. Only few experimental works studying this problem exist in the literature [9–12]. The related computational fluid dynamics (CFD) literature has been mainly devoted to the study of the DS phenomenon whereas the majority of the work deals with airfoil configurations. Ekaterinaris and Platzer [13] reviewed the CFD simulations of airfoil DS up to 1996. The 3-D DS of the laminar flow around a NACA0015 wing was then simulated by Newsome [14], where little emphasis was given to the behavior of the tip vortex under DS conditions. Szydlowski and Costes [15] used RANS and DES methods to simulate the flow around a NACA0015 airfoil under static and dynamic stall. Their work was focused on the prediction of the stall condition over the airfoil geometry. Their main conclusion was the immaturity of their then modeling capabilities to predict static and dynamic stall conditions. In a recent work by Spentzos et al. [16], the 3-D DS of turbulent flows around oscillating wings with various platforms was studied using a RANS methodology. A good agreement between CFD and experimental results was reported in their work. They also investigated the interaction of the tip vortex with the DS vortices over the wing platform. However, no information was provided regarding the downstream evolution of the tip vortex behind the wing.

The objective of this work is twofold. First, DES and RANS methods are evaluated to predict the onset of static and dynamic stall. Second, the downstream evolution of the tip vortex under DS oscillations is investigated. Throughout this study, RANS and DES results are compared with each other as well as the experimental data of Birch and Lee [11,12] for a square NACA0015 wing. The mathematical and numerical models are described in the next section. The DES calibration and the simulation results for stationary and oscillating wings are presented in Sec. III. Conclusions and plans for future work are given at the end.

II. Methodology

A. Mathematical Models

The unsteady turbulent aerodynamic flow is modeled by compressible NS equations. Turbulence effects are taken into account via an eddy-viscosity approach, whereby the kinematic viscosity and thermal conductivity, μ and k, are augmented by modeled turbulent (eddy) viscosity and turbulent thermal conductivity, μ_t and k_t, respectively. Molecular diffusion parameters μ and k are then replaced by $\mu + \mu_t$ and $k + k_t$ in the NS equations. Turbulent thermal conductivity is calculated from turbulent viscosity with the assumption of a constant turbulent Prandtl number of $Pr_t = (c_p \mu_t / k_t) = 0.9$.

The closure is achieved by solving the one-equation SA turbulence model [17] for the reduced eddy viscosity, $\tilde{\nu}$. The transport equation is given by

$$\frac{D(\rho\tilde{\nu})}{Dt} = c_{b1}\rho\tilde{S}\,\tilde{\nu} + \frac{1}{\sigma}\nabla\cdot[(\rho\nu + \rho\tilde{\nu})\nabla\tilde{\nu}] + \frac{c_{b2}}{\sigma}\rho(\nabla\tilde{\nu})^2 - c_{w1}\rho f_{w1}\left(\frac{\tilde{\nu}}{d}\right)^2 \tag{1}$$

Variables and functions presented in Eq. (1) are defined as

$$\nu_t = \tilde{\nu} f_{v1}, \qquad f_{v1} = \frac{\chi^3}{\chi^3 + c_{v1}^3}, \qquad \chi = \frac{\tilde{\nu}}{\nu}$$

$$\tilde{S} = S + \frac{\tilde{\nu}}{\kappa^2 d^2} f_{v2}, \qquad f_{v2} = 1 - \frac{\chi}{1 + \chi f_{v1}}$$

$$f_w = g\left(\frac{1 + c_{w3}^6}{g^6 + c_{w3}^6}\right)^{1/6}, \qquad g = r + c_{w2}(r^6 - r), \qquad r = \frac{\tilde{\nu}}{\tilde{S}\kappa^2 d^2}$$

where constants c_{b1}, c_{b2}, c_{w1}, c_{w2}, c_{w3}, c_{v1}, and κ have the same values as those indicated by Spalart and Allmaras [17].

In the course of the LES calibration as described in the next section, we have also implemented a Smagorinsky subgrid scale (SGS) model where the turbulent viscosity is given by an algebraic relation,

$$\nu_t = (C_S \Delta)^2 \parallel S \parallel \tag{2}$$

For the treatment of moving or deformable meshes, governing equations of the flow and turbulent viscosity are reformulated based on the arbitrary Lagrangian–Eulerian kinematical description of the fluid domain [18].

B. Computational Methods

1. Space-Time Discretization

The flow equations are discretized with a hybrid finite volume/finite element method [19], which is accompanied by the discretization of the computational domain into unstructured tetrahedral elements and the construction of median-dual control volumes around mesh vertices. Convective fluxes are calculated using the second-order upwind Roe scheme whereas diffusive terms are discretized with linear finite element shape functions. The spatially discretized formulation of the compressible Navier–Stokes equations can be written as

$$\begin{cases} \text{find } \mathbf{U}_h \in \mathbf{\Phi}_h \text{ such that} \\ \int_{C_I} \frac{\partial \mathbf{U}_h}{\partial t}\,\mathrm{d}\Omega + \int_{\partial C_I} \mathbf{F}\cdot\mathbf{n}\,\mathrm{d}\Gamma = \int_{\Omega_h} \nabla\cdot\mathbf{G}\phi_I\,\mathrm{d}\Omega \quad \forall\ \phi_I 1 \le I \le N \end{cases} \tag{3}$$

where $\mathrm{d}\Omega$ is an infinitesimal volume of the median-dual control volume C_I and $\mathrm{d}\Gamma$ is an infinitesimal surface area of the control volume boundary surface. Ω_h is the tetrahedral discretization of the computational domain and ϕ_I is the linear finite element shape function associated with node I. A two-dimensional triangularization of the computational domain and the corresponding median-dual control volumes are depicted in Fig. 1.

The vector of conservative variables $\mathbf{U}$ and convective and viscous flux functions $\mathbf{F}$ and $\mathbf{G}$ are given by

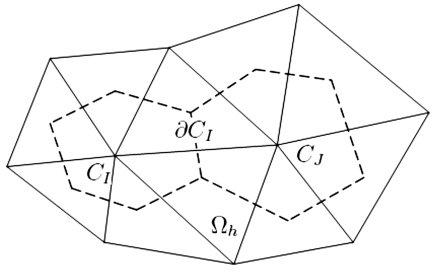

Fig. 1 Two-dimensional triangularization of the computational domain and the median-dual control volumes built around each mesh vertex.

$$\mathbf{U}^T = [\rho \quad \rho u \quad \rho v \quad \rho w \quad \rho E] \tag{4}$$

$$\mathbf{F} = \begin{bmatrix} \rho u & \rho v & \rho w \\ \rho u^2 + p & \rho v u & \rho w u \\ \rho u v & \rho v^2 + p & \rho w v \\ \rho u w & \rho v w & \rho w^2 + p \\ \rho u H & \rho v H & \rho w H \end{bmatrix} \tag{5}$$

$$\mathbf{G}^T = \begin{bmatrix} 0 & \tau_{xx} & \tau_{yx} & \tau_{zx} & \tau_{xx}u + \tau_{yx}v + \tau_{zx}w + (\frac{\gamma\mu}{Pr} + \frac{\gamma\mu_t}{Pr_t})\frac{\partial e}{\partial x} \\ 0 & \tau_{xy} & \tau_{yy} & \tau_{zy} & \tau_{xy}u + \tau_{yy}v + \tau_{zy}w + (\frac{\gamma\mu}{Pr} + \frac{\gamma\mu_t}{Pr_t})\frac{\partial e}{\partial y} \\ 0 & \tau_{xz} & \tau_{yz} & \tau_{zz} & \tau_{xz}u + \tau_{yz}v + \tau_{zz}w + (\frac{\gamma\mu}{Pr} + \frac{\gamma\mu_t}{Pr_t})\frac{\partial e}{\partial z} \end{bmatrix} \tag{6}$$

The SA turbulence model equation (1) is discretized similar to the flow equations. Convective and temporal terms are calculated using the median-dual finite volume approach, while diffusive, anti-diffusive, source, and sink terms are discretized using linear finite element shape functions. NS and SA equations are loosely coupled during the computation, that is, NS equations are solved first, then turbulence viscosity is updated using recently calculated values of the flow variables.

The time integration is performed via a second-order accurate implicit scheme, and the nonlinear fluxes are linearized by applying the Newton method and introducing flux Jacobian matrices. Geometric conservation laws developed by Lesoinne and Farhat [20] and Farhat et al. [21] are implemented for the time integration of the convective fluxes in moving or deformable meshes while the corresponding Jacobians are calculated at the intermediate mesh positions described by Nkonga and Guillard [22]. Since the construction of a spatially second-order accurate convective Jacobian is difficult, only a first-order approximation is used. For time accurate unsteady simulations, the spatial accuracy is then improved by performing two or three Newton iterations at each time step [23].

2. *Iterative Solver and Preconditioning*

The linear system of equations resulted from aforementioned discretization schemes is solved with a preconditioned (block Jacobi) generalized minimal residual method (GMRES) [24]. To improve the convergence of the flow solver at low Mach numbers, the local low-speed preconditioner of Turkel and Vatsa [25] is implemented. The preconditioning matrix for the entropy variables $\mathbf{W}^T = [p, u, v, w, \hat{S}]$ is given by

$$\mathbf{P}_e = \begin{bmatrix} \beta^2 & 0 & 0 & 0 & 0 \\ 0 & 1 & 0 & 0 & 0 \\ 0 & 0 & 1 & 0 & 0 \\ 0 & 0 & 0 & 1 & 0 \\ 0 & 0 & 0 & 0 & 1 \end{bmatrix} \tag{7}$$

where β is the local Mach number. The low-speed modifications for the Roe scheme (Roe–Turkel scheme [26]) are performed at two levels: preconditioning of the temporal term (iterative preconditioning) and preconditioning of the upwind term. The first stage enhances the convergence rate, and the second improves the accuracy of the solution at low Mach numbers. To preserve the time accuracy required for unsteady flow simulations, the low-speed preconditioning is always performed in the context of multiple Newton iterations per time step.

3. *Detached-Eddy Simulation*

The delayed DES (DDES) model of Spalart et al. [8] based on the SA Eq. (1) is implemented in the flow solver. SA-DDES and its older version SA-DES97 [1] are built by replacing the distance to the solid wall, d, in Eq. (1) with a smaller length scale $\tilde{d}$. This modification results in a bigger destruction term and hence reduces the modeled turbulent viscosity, ν_t, in the separated regions and away from the solid wall where the flow is dominated by 3-D vortical structures (LES regions). In DDES, $\tilde{d}$ is given by [8]

$$\tilde{d} = d - f_d \max(0, d - C_{\text{DES}}\Delta) \tag{8}$$

The value of constant C_{DES} will be determined, in the next section, by simulating the decay of isotropic turbulence (DIT) in a periodic box and calibrating the simulation results with the available direct numerical simulation (DNS) data. The function f_d should be around 1 in the LES region and almost 0 in the attached boundary-layer (RANS region) as well as irrotational zones. Its value depends on the nondimensional parameter r_d. The parameter and the function are defined by Spalart et al. [8] as

$$r_d = \frac{\tilde{\nu}}{\sqrt{U_{i,j}U_{i,j}}\kappa^2 d^2} \tag{9}$$

$$f_d = 1 - \tanh(8^3 r_d^3) \tag{10}$$

For each mesh vertex (control volume), the length scale Δ is defined, herein, as the length of the longest edge connected to this vertex. In unstructured median-dual control volumes, this represents the largest distance between the center of the control volume under consideration and the center of its neighboring control volumes.

The numerical dissipation of upwind methods tends to impair the resolution of the turbulence coherent structures by strongly dissipating the turbulent kinetic energy in medium size eddies. The common practice is to scale down the amount of the numerical dissipation of the scheme in the LES regions. Travin et al. [6] developed a blending function that allows upwind formulation to be active in high vorticity and fine grid areas, whereas Barone and Roy [5] used Harten's artificial compression method to adjust the magnitude of the numerical dissipation. In this paper, the upwind part of the Roe–Turkel flux is scaled as follows:

$$\mathbf{F}^{ij}_{\text{Roe}} = \tfrac{1}{2}(\mathbf{F}_i + \mathbf{F}_j) - \tfrac{1}{2}\sigma\mathbf{P}_c^{-1}|\mathbf{P}_c\mathbf{A}|(\mathbf{U}_j - \mathbf{U}_i) \tag{11}$$

where the scaling parameter σ is obtained from function f_d as

$$\sigma = 1 - f_d \tag{12}$$

In the next section, a slightly modified version of relation (12) will be introduced. All numerical algorithms described in this section are parallelized using the message passing standard.

III. Results

A. Decay of Isotropic Turbulence: Calibration of Large-Eddy Simulation Mode

The simulation results for the decay of isotropic turbulence in a periodic box is compared with the DNS data of the AGARD LES validation database.[§] The computational domain consisted of a cube with equal edge lengths of 2π. Periodic boundary conditions were applied to each of three pairs of facing sides of the cube. As depicted in Fig. 2, the initial flowfield inside the box consisted of isotropic vortices which would decay in the course of simulations. Two different mesh resolutions were studied: the coarse and fine meshes contained 32^3 and 64^3 uniform cubes, respectively. Each cube was then divided into six tetrahedral elements. Comparisons were made between the calculated 3-D energy spectra at a nondimensional time of 2.018.

The calibration steps described by Bunge et al. [7] were followed. First, the calibration was performed for the Smagorinsky model, whereby the optimal value for constant C_s as well as upwinding parameter σ was obtained. The upwinding parameter in Eq. (11) was kept constant throughout the computational domain. As depicted in

[§]Jiminez, J., "A Selection of Test Cases for the Validation of Large-Eddy Simulations of Turbulent Flows," ftp://torroja.dmt.upm.es/AGARD/ [retrieved March 2008].

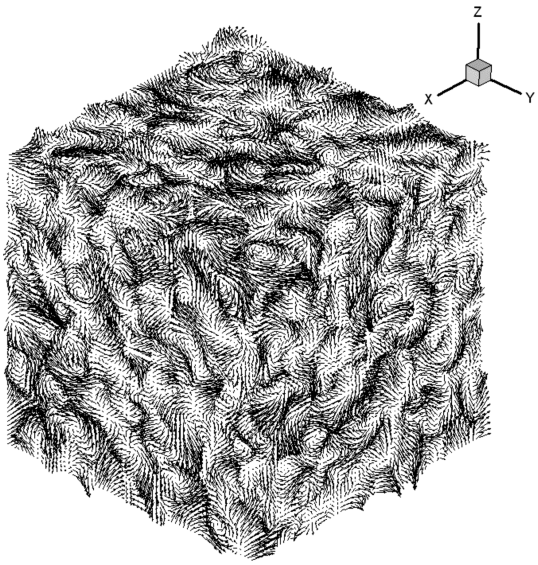

Fig. 2 Vector plot of the initial solution in the DIT cube.

Fig. 3a, $\sigma = 0.015$ was the optimal value for the 64^3 resolution with $C_s = 0.15$. The optimal value of C_s was strongly dependent on the grid resolution. For the coarse mesh, $C_s = 0.19$ gave the best result.

At the second stage, detached-eddy simulations were performed where the SA turbulence model replaced the Smagorinsky SGS model. The proper initialization of the turbulence viscosity field was achieved as follows [7]: the Smagorinsky model was used to obtain the initial guess for the distribution of the eddy viscosity in the domain. The SA equation was then solved while the flowfield was kept frozen until convergence. The DIT simulation followed thereafter. The turbulent 3-D energy spectra at various C_{DES} constants are shown in Fig. 3b. Unlike the Smagorinsky constant, C_{DES} is less sensitive to the grid resolution. We have selected $C_{\mathrm{DES}} = 0.51$ as the optimal value. Finally, another simulation was performed in which C_{DES} was kept at its optimal value while the upwinding parameter was calculated from Eq. (12) and limited as

$$\sigma = \max(0.015, 1 - f_d) \tag{13}$$

The energy spectra and flowfield were similar to those with constant value of $\sigma = 0.015$. This indicated the proper behavior of the function f_d, which took values close to 1 in the entire DIT box (LES region).

The second norm of the residual was reduced up to six orders of magnitude in GMRES iterations. Two Newton iterations were performed at each time step. Increasing the number of Newton iterations had no significant results in the time evolution of the turbulent 3-D energy spectra.

B. NACA0015 Wing

1. *Overview*

The structure of the tip vortex generated by a square NACA0015 wing was numerically studied using RANS and DES methods. The problems considered include the stationary wing fixed at various angles of attack (AOA) and the wing in pitching oscillations. These problems were experimentally investigated by Birch and Lee [11,12]. They measured velocity components at grid points with uniform spacing of 3.2 mm on a rectangular plane located at $x/c = 1$. In our numerical study, we interpolated the velocity components on similar grid points from the simulated flowfield. Our purpose is to compare the performance of RANS and DES models to predict the near-field structure of the tip vortex and the onset of the static and dynamic stall. For the vortex visualization in the 3-D flowfield, we adopted the λ_2 method of Jeong and Hussain [27].

2. *Wing Configuration and Mesh*

The test case consisted of a rectangular, square-tipped NACA0015 half-wing with chord and half-span sizes of 0.203 and 0.508 m, respectively. The wing was attached to a free-slip wall at the root section. This geometry was slightly different from the one used for experimental studies where the root was attached to an endplate, which, in turn, was located close to the wind-tunnel wall [11,12]. The wing configuration is depicted in Fig. 4. The origin of the Cartesian coordinate system was placed at the trailing edge of the wing at the tip section with its x and z axes along the chord line and the span of the wing, respectively. For the oscillating wing, the above orientation corresponded to the wing at the mean incidence angle. The pitching axis passed through the quarter-chord points and was parallel to the z axis.

The freestream velocity was equal to 14.4 m/s, which resulted in a chord Reynolds number of 1.86×10^5. The stationary simulations were performed at four AOAs of $\alpha = 12.0$, 14.0, 16.0, and 18.0 deg; whereas, the nonstationary simulation involved pitching oscillations with a reduced frequency of 0.09, a mean incidence angle of 18.0 deg, and an amplitude of 6.0 deg, that is, $\alpha = 18.0 + 6.0 \deg \sin(\omega t)$.

The computational mesh shown in Fig. 4 contained 2,247,174 nodes and 13,300,570 tetrahedral elements. As described by Spalart [28], the computational domain was divided into several target regions addressing different modeling schemes. Tetrahedral

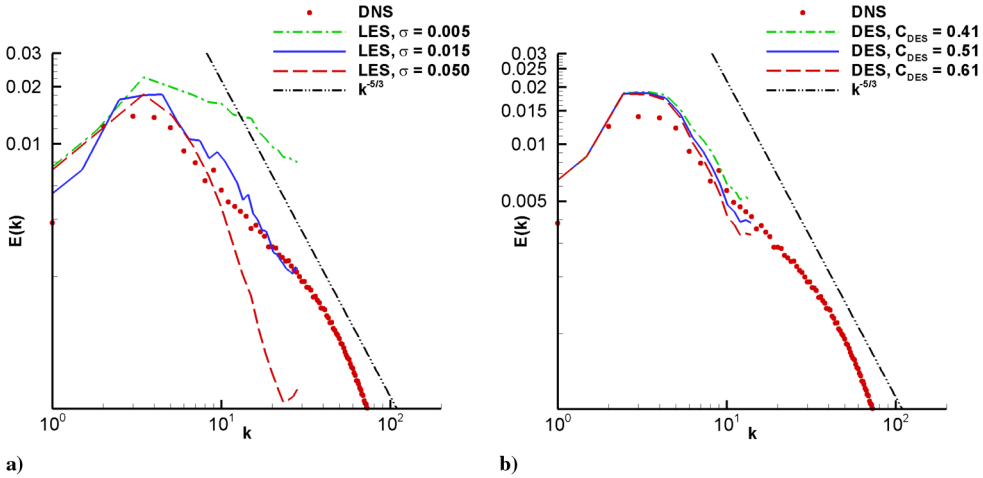

Fig. 3 Calibration of parameters in Smagorinsky LES and DES schemes with DNS data (Jiminez, J., "A Selection of Test Cases for the Validation of Large-Eddy Simulations of Turbulent Flows," ftp://torroja.dmt.upm.es/AGARD/ [retrieved March 2008].) for the DIT problem. a) 3-D energy spectra in a 64^3 cube at a nondimensional time of 2.018 at different values of the upwinding parameter using the Smagorinsky SGS model with $C_s = 0.15$. b) 3-D energy spectra in a 32^3 cube at a nondimensional time of 2.018 at different values of the C_{DES} parameter using the DES model with $\sigma = 0.015$.

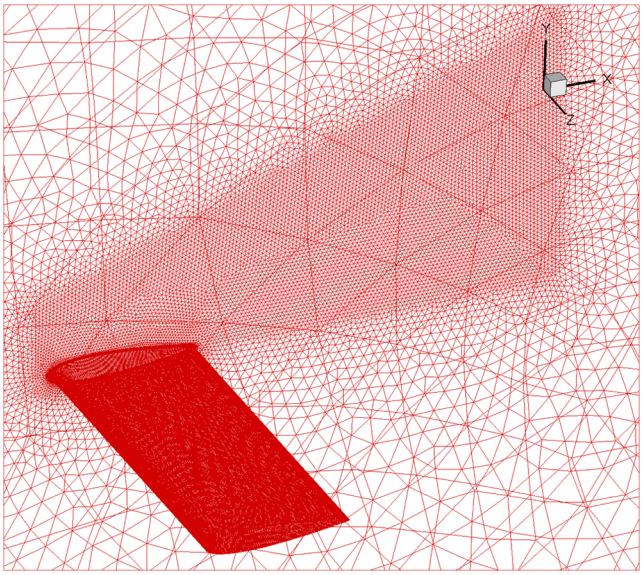

Fig. 4 Unstructured tetrahedral mesh around the NACA0015 wing with 2,247,174 nodes and 13,300,570 elements. The focus region of DES appears in the figure as the dense trapezoidal region above the wing, which contains 5,308,217 elements.

elements were constructed by triangulation of semistructured prism layers in the RANS region. The grid spacing from the wall in the first layer satisfied $y^+ \approx 1$ in the law-of-wall units. The focus region (FR), which can be distinguished, in Fig. 4, as the dense area above the wing, contained an almost isotropic mesh with a uniform edge size of $0.028c$. This region was connected to an Euler region (ER) through a small departure region. The maximum size of the mesh edges in the ER was limited to c. A finer grid with 4,379,053 nodes and 26,064,193 tetrahedra was built via grid refinement by a factor of $\sqrt{2}$ in the FR to examine whether the coarse simulation results were sufficiently resolved. The time step for the stationary and oscillating wing simulations was $0.0078c/U_\infty$. The coarse and fine grids were decomposed into 46 and 64 subdomains using METIS [29]. Although RANS requirements for mesh and time step are generally less stringent than DES's, the same mesh and time step were used for RANS simulations to make a fair assessment of the accuracy of each scheme for unsteady flow simulations.

3. *Stationary Wing*

Figure 5 compares DES results to RANS solutions for the static wing at $\alpha = 18$ deg. Both simulations were performed on the coarse grid. DES, Fig. 5a, predicted a completely detached flow from almost the whole area of the wing upper surface leading to the vortex shedding. RANS, Fig. 5b, failed to predict the shedding of vortices. However, a strong trailing-edge vortex was resolved with a flow reversal that extended from the trailing edge up to $0.2c$ in the inboard region, Fig. 6a. The velocity vector plot obtained from DES is shown in Fig. 6b, where the shedding of vortices is clearly visible. The flow detachment or reversal gradually diminished toward the wing tip in DES and RANS solutions. Furthermore, due to the excessive dissipation, the RANS model predicted a thicker and more diffused tip vortex, as depicted in Fig. 5. The $x/c = 1$ data plane crossing the tip vortex is depicted in the same figures.

2-D vorticity contours at the $x/c = 1$ plane are compared in Fig. 7. DES results were averaged over 100 time steps. The peak value of nondimensional vorticity calculated in the experiment [12] was 23. Here again RANS predicted a significantly lower value for the maximum vorticity.

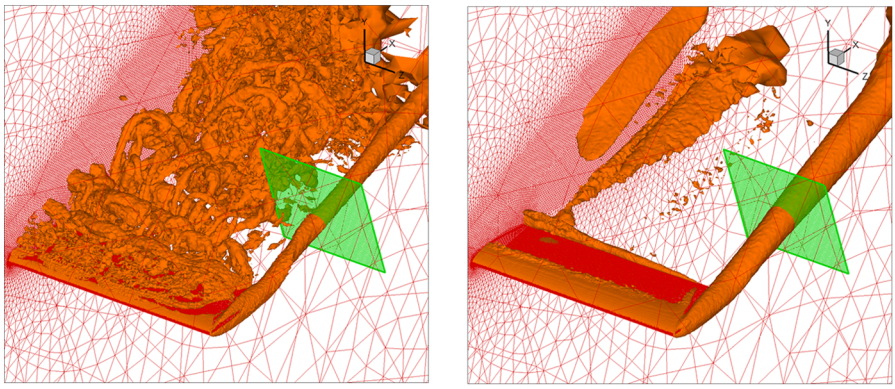

a) **b)**

Fig. 5 λ_2 isosurfaces in flow around the stationary NACA0015 wing at $\alpha = 18$ deg. a) DES results; b) RANS results.

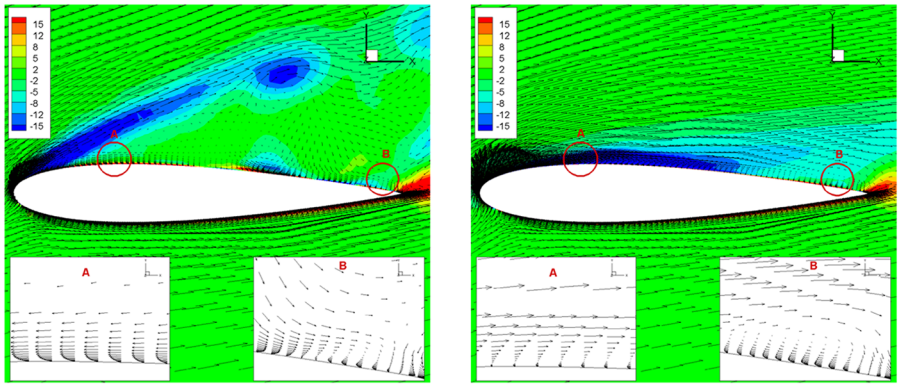

a) **b)**

Fig. 6 Vector and vorticity contour ($\zeta c/U_\infty$) plots at the root section for the flow around a stationary NACA0015 wing at $\alpha = 18$ deg. a) DES results; b) RANS results.

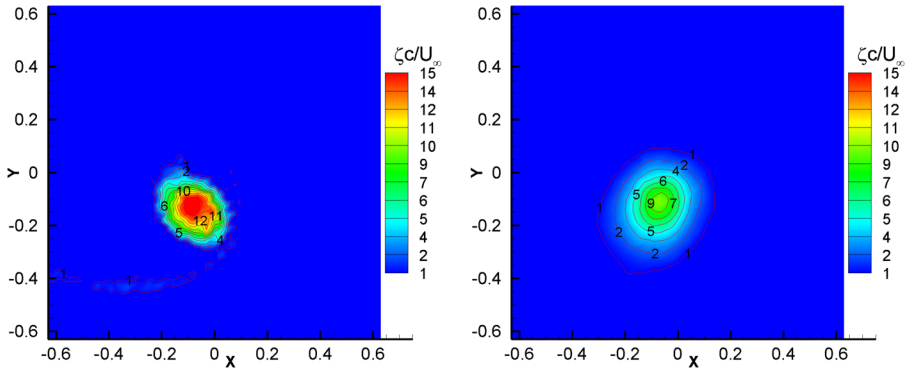

Fig. 7 Vorticity contours at the $x/c = 1$ plane for the flow around a stationary NACA0015 wing at $\alpha = 18$ deg. a) DES results; b) RANS results.

The onset of the static stall is investigated in Figs. 8a–8f, where the vortex field around the NACA0015 wing is shown at three static AOAs of 12, 14, and 16 deg. At $\alpha = 12$ deg, Figs. 8a and 8b, the flow was entirely attached to the wing surface. The flow separation at the trailing edge and the resulting trailing-edge vortex were observed at $\alpha = 14$ deg in Figs. 8c and 8d. Further increase of the AOA to 16 deg led to the appearance of different flow structures in the DES and RANS results. Although the massive separation of the flow over the

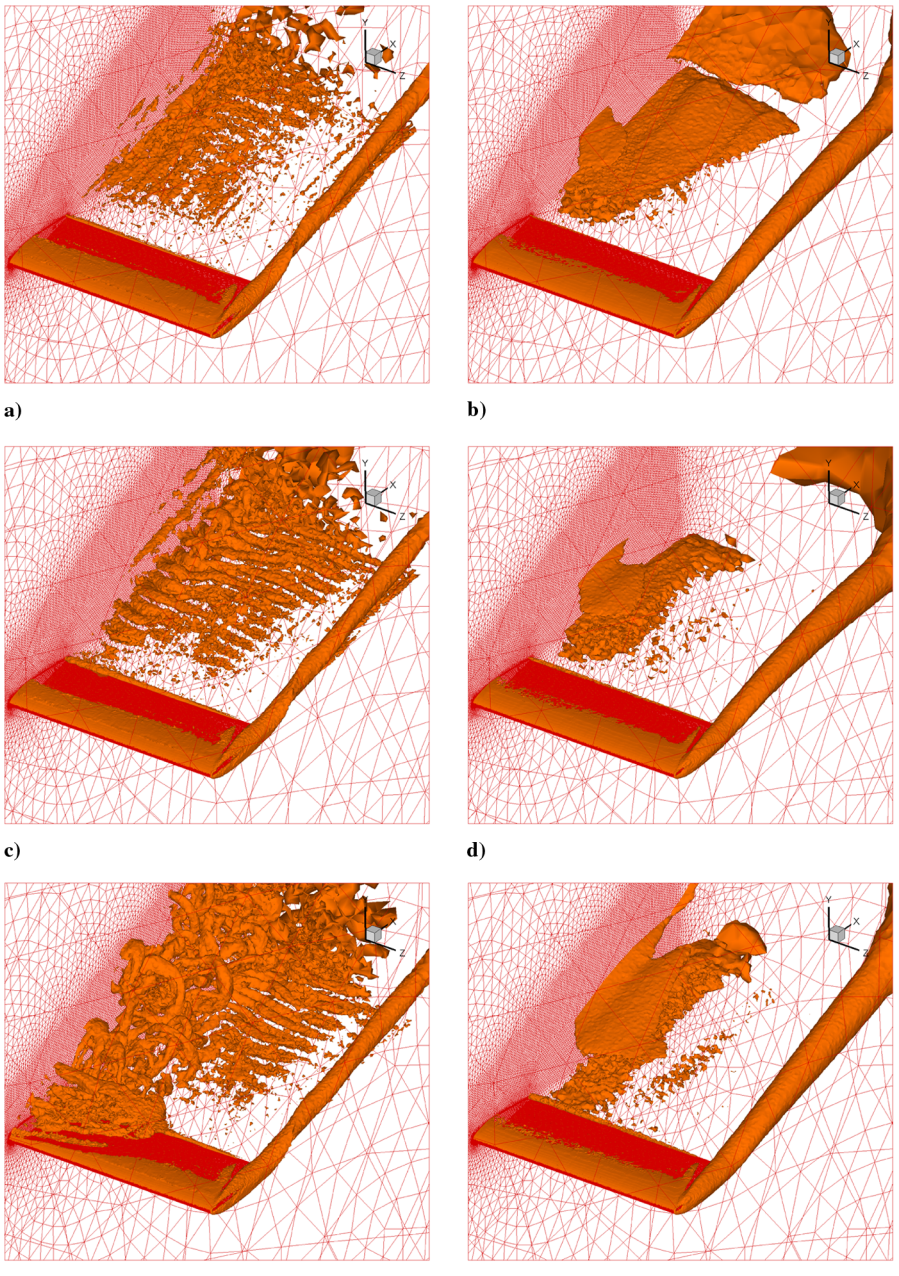

Fig. 8 λ_2 isosurfaces around a static NACA0015 wing at three AOAs of 12, 14, and 16 deg. a) DES at $\alpha = 12$ deg; b) RANS at $\alpha = 12$ deg; c) DES at $\alpha = 14$ deg; d) RANS at $\alpha = 14$ deg; e) DES at $\alpha = 16$ deg; f) RANS at $\alpha = 16$ deg.

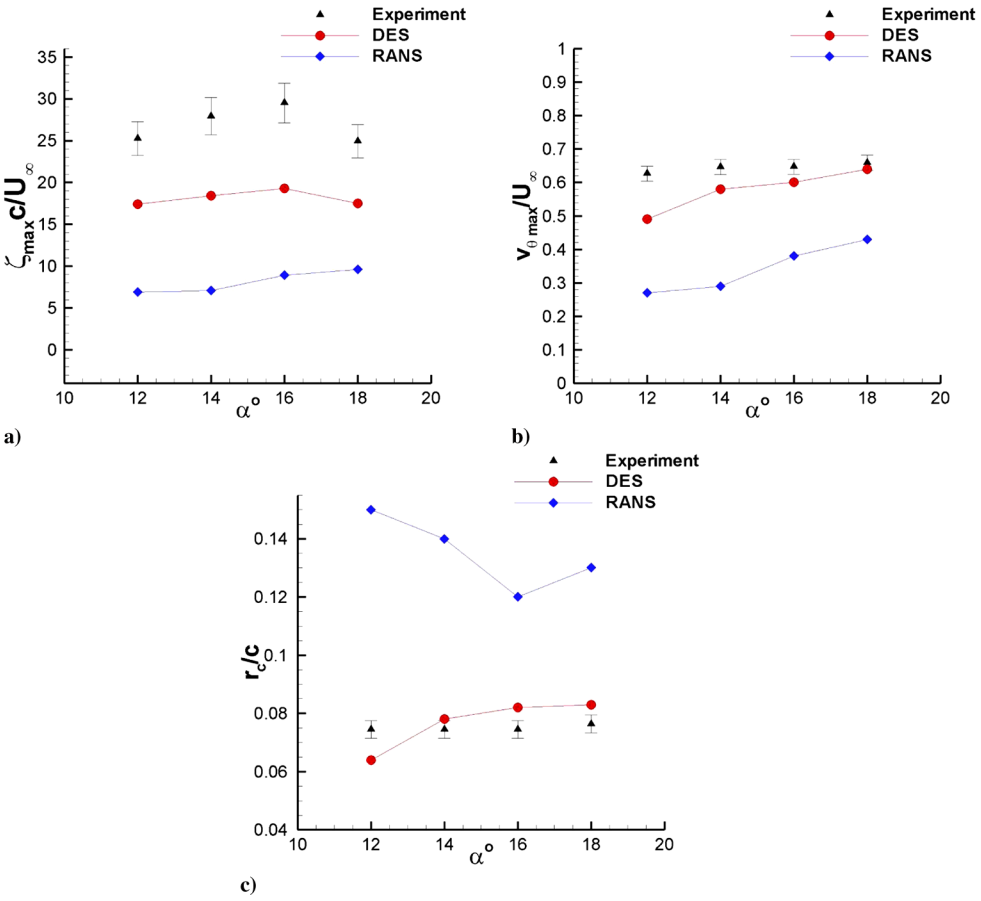

Fig. 9 Variation of vortex parameters with AOA at the $x/c = 1$ plane and comparison with the experimental data [11] for the flow around a stationary NACA0015 wing. a) Maximum vorticity; b) maximum tangential velocity; c) core radius.

inboard part of the wing upper surface and the vortex shedding were revealed by DES in Fig. 8e, RANS simulations only showed a bigger trailing vortex without any extensive flow separation or shedding of vortices, Fig. 8f. The approximate static stall AOA predicted by DES would therefore lie between 14 and 16 deg, that is, $14 < \alpha_{ss} < 16$ deg. This complies with the experimental measurement [12] in which $\alpha_{ss} \approx 15$ deg, whereas RANS results depicted in Figs. 5 and 8 imply that $16 < \alpha_{ss} < 18$ deg.

Maximum vorticity, maximum tangential velocity, and vortex core radius versus four angles of attack at $x/c = 1$ plane are shown in Fig. 9. The core radius was measured as the distance between the location of the maximum tangential velocity and the center of the vortex. DES results for all three parameters lie between RANS solutions and the experimental data [11]; a significant improvement was obtained to better predict the tip-vortex configuration at $x/c = 1$.

DES was, on average, 4 times slower than RANS in the reported simulations. As depicted in Fig. 10, in DES, the iterative solver performed almost 3.5 times more iterations to reduce the residual 8 orders of magnitude at each time step.

4. *Oscillating Wing*

The dynamic stall of the NACA0015 wing in pitching oscillations was simulated. The reported simulations in this section were performed on the coarse grid. Before the presentation of the results, two points should be clarified as follows:

1) A phase-lag compensation scheme was employed in the experimental studies of Birch and Lee [11,12] to modify the instantaneous position of the wing at the moment of the flow measurement. This compensation was intended to take into account the phase lag that exists for the flow structure to move from the wing to the location of the velocity sensors ($x/c = 1$ plane). In this section, whenever we examine only simulation results (DES and/or RANS), the reported wing angles are not compensated. This helps us investigate the vortex flow structure during the oscillation cycle without being involved with the discrepancies that exist between different compensation schemes. Whereas in the graphs that include comparisons between simulation and experimental data, for the sake of consistency, the same phase-lag compensation scheme as the one used by Birch and Lee was implemented. The compensated angles are enclosed within the parentheses in the text.

2) The simulation results presented in this section are instantaneous quantities calculated at various wing positions. The reported experimental data were, on the contrary, the ensemble averages over 40–80 pitching cycles at the corresponding positions. In DES,

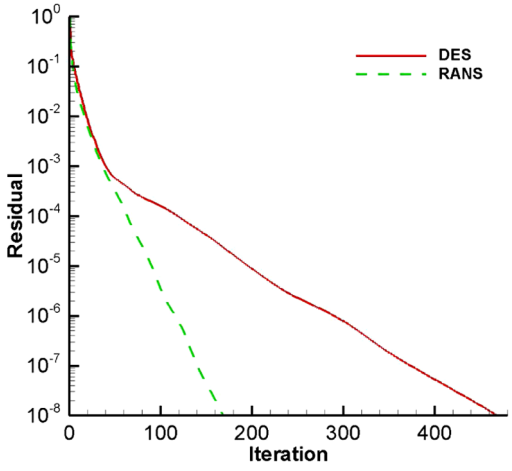

Fig. 10 GMRES residual versus number of iterations in a typical time step for DES of the stationary wing at $\alpha = 16$ deg.

calculating the phase-locked averages of the flow quantities even over a few cycles is computationally very expensive (each DES cycle takes more than 3 weeks with our current computational resources). Although RANS simulations are significantly less expensive than DES, the calculated flow quantities exhibited very little changes over different cycles except for the first transient quarter cycle. Because of the high computational cost for DES and the lack of the significance for RANS, only the instantaneous flow quantities at specified wing positions were presented.

The structure of the tip vortex and turbulent eddies resulted from the flow separation in DES and RANS solutions are shown in Figs. 11 and 12a–12e, where pitch-up and pitch-down strokes are distinguished by subscripts u and d, respectively. Turbulent eddies in RANS solutions, similar to the static wing simulation, were highly diffused. The excessive numerical diffusion impaired the resolution of small eddy structures. The numerical diffusion merged the small eddies into each other and cloudlike structures were formed in RANS solutions. The strong tip vortex was also diffused and had a larger diameter when compared to the DES solution.

The following unsteady flow behaviors were observed for the DES in a pitching cycle: during the pitch up from $\alpha = 12_u$ deg to $\alpha = 16_u$ deg (15.1_u deg), the flow was mainly attached, Fig. 11a. A small region of the flow reversal appeared at the inboard area of the wing trailing edge at the end of this period, Fig. 11b. This flow reversal expanded more toward the outboard region and the leading edge from $\alpha = 16_u$ deg (15.1_u deg) to $\alpha = 22_u$ deg (21.4_u deg), Fig. 11c. Meanwhile, the leading-edge vortex was formed and grew up. The dynamic stall started at $\alpha \approx 22_u$ deg (21.4_u deg), which was characterized by the massive separation region covering most of the wing upper surface, Fig. 11d. The dynamic stall condition continued until $\alpha \approx 20_d$ deg (20.9_d deg). The flow reattachment began afterward, Fig. 11e, and proceeded gradually until the complete reattachment of the flow at the lower peak of the pitching cycle. The DES prediction of the deep-stall oscillation was in good agreement with the reported experimental observation [11]. RANS predictions are depicted in Figs. 12a–12e, where more or less the same qualitative behaviors for the onset of the flow separation and reattachment were observed. The massive separation region in

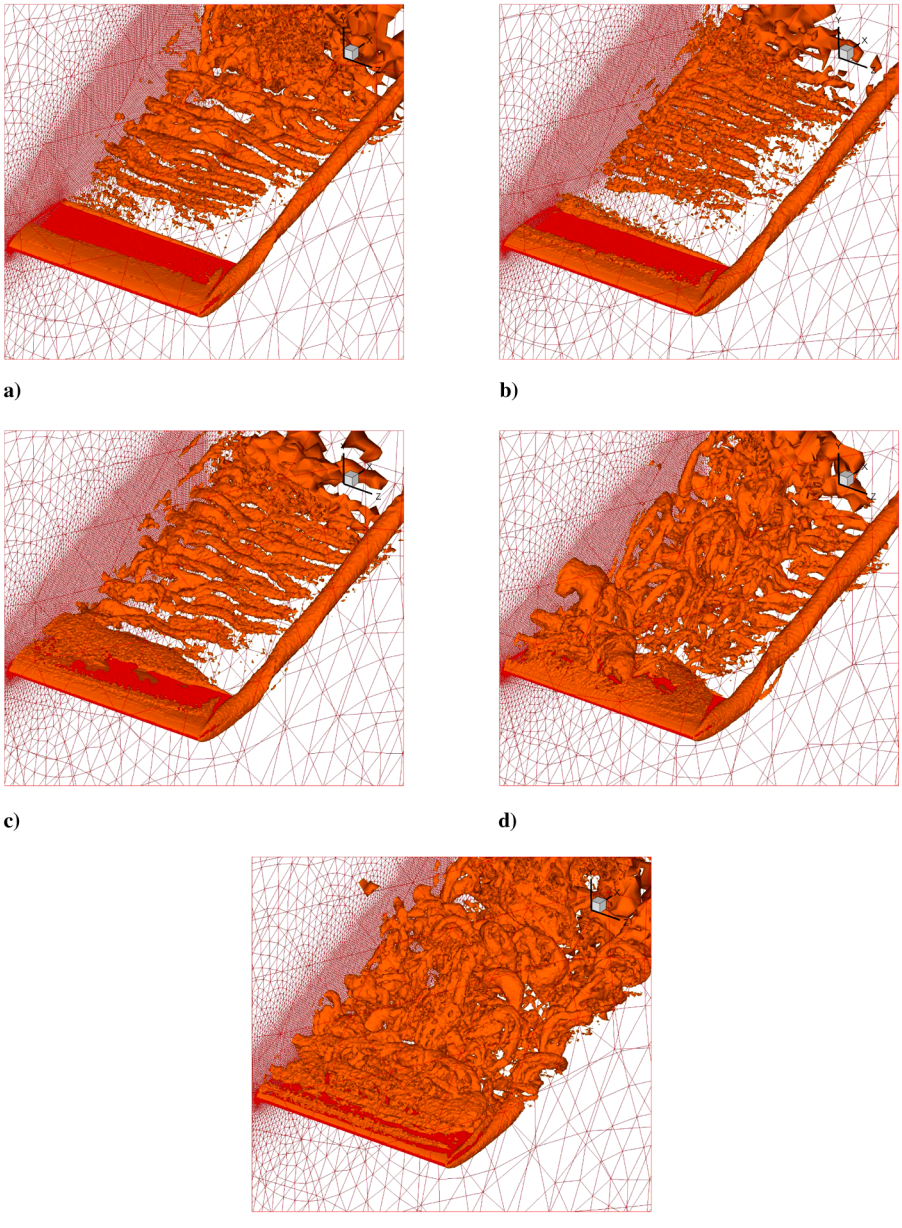

Fig. 11 DES predictions for λ_2 isosurfaces around an oscillating NACA0015 wing at various pitching angles, $\alpha = 18 + 6$ deg $\sin(\omega t)$. a) $\alpha = 12_u$ deg; b) $\alpha = 16_u$ deg; c) $\alpha = 19_u$ deg; d) $\alpha = 22_u$ deg; e) $\alpha = 18_d$ deg.

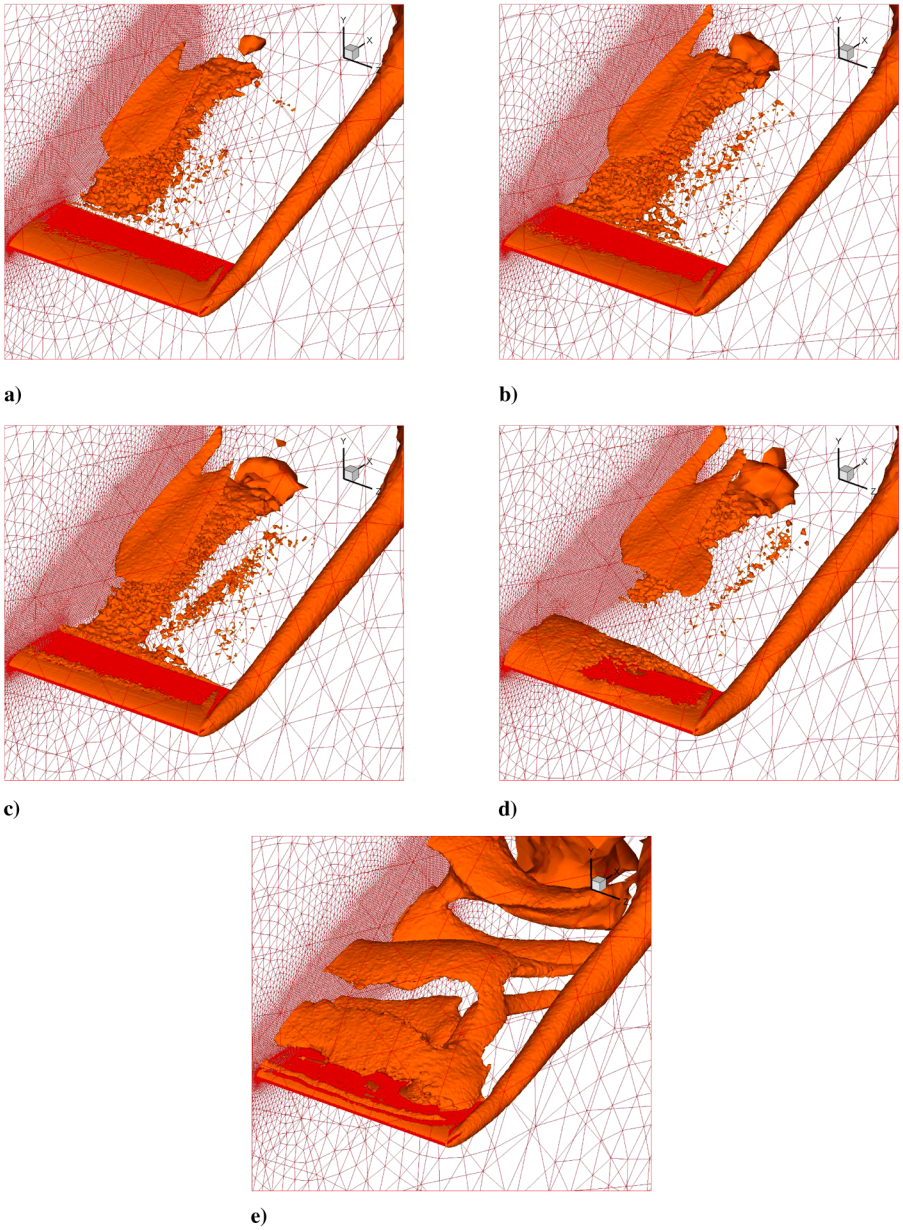

Fig. 12 RANS predictions for λ_2 isosurfaces around an oscillating NACA0015 wing at various pitching angles, $\alpha = 18 + 6\ \text{deg}\sin(\omega t)$. a) $\alpha = 12_u$ deg; b) $\alpha = 16_u$ deg; c) $\alpha = 19_u$ deg; d) $\alpha = 22_u$ deg; e) $\alpha = 18_d$ deg.

RANS, Fig. 12d, was more limited to the inboard part of the wing and smaller than the similar region in DES. Table 1 compares DES, RANS, and experimental results [11] in terms of the compensated phase angle intervals during which the flow separation, stall, and reattachment take place. The conversion table reported by Birch and Lee [11] was used to obtain compensated angles from corresponding wing phase angles; for example, the compensated phase angle of 21.4_u deg in Table 1 corresponds to a wing phase angle of 22_u deg in simulations.

Furthermore, DES predicted the breakup of the tip vortex, which began during the pitch up between 23_u deg (22.6_u deg) and 24 deg (23.9_u deg). The tip vortex was restored to its original uniform structure much later at $\alpha \approx 16_d$ deg (16.9_d deg). The distorted tip vortex during the pitch down at $\alpha = 18_d$ deg (19.0_d deg) is depicted in Fig. 11e. RANS failed to capture this breakup. Because only velocity components of the flow were measured on some fixed data planes corresponding to different x/c locations in the experimental study, the vortex breakup was not explicitly reported by Birch and Lee. However, the effect of it was seen and pointed out in the phase-locked ensemble averaged data as the highly diffused vortex, the lack of axisymmetry, and lower values of vorticity.

Table 1 Comparison between DES, RANS, and experimental data for compensated phase angle intervals corresponding to different flow regimes in a pitching cycle

Flow regime	DES	RANS	Experiment
Attached flow	12.0_u–15.1_u	12.0_u–16.0_u	12.0_u–14.5_u
Separation and vortex growth	15.1_u–21.4_u	16.0_u–22.6_u	14.5_u–22.0_u
Dynamic stall	21.4_u–20.9_d	22.6_u–20.0_d	22.0_u–20.0_d
Reattachment	20.9_d–12.0_d	20.0_d–12.0_d	20.0_d–12.0_d

The contour plots of the tangential velocity at $\alpha = 22_u$ deg and 16_d deg (21.40_u deg and 16.87_d deg) on the $x/c = 1$ plane are shown in Fig. 13. DES results revealed a significant change in the tip-vortex configuration between these two angles, Figs. 13a and 13b. At 16_d deg the vortex is still recovering from the breakup, while the RANS vortex did not experience a prominent evolution during this oscillation interval as depicted in Figs. 13c and 13d, where a strong vortex core is present at both phase angles.

The dynamic loops of the peak vorticity level, peak tangential velocity, and vortex core radius at the $x/c = 1$ plane are shown in Figs. 14a–14c, respectively, and compared with the available experimental data. The abscissa represents the compensated angles

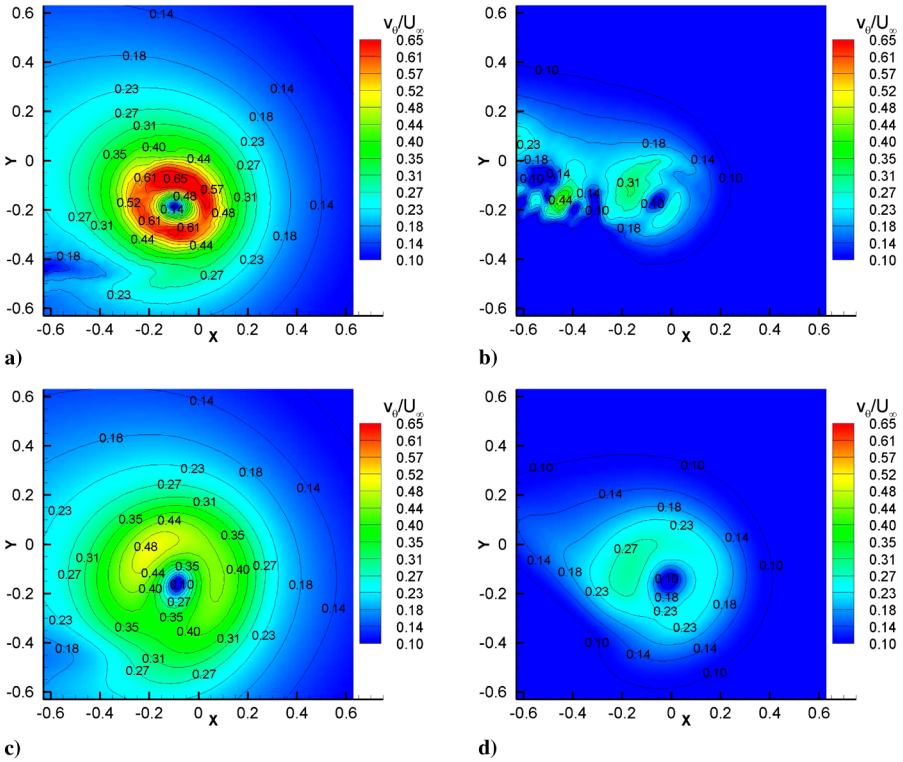

Fig. 13 Tangential velocity contours at the $x/c = 1$ plane for the flow around the oscillating NACA0015 wing with $\alpha = 18 + 6 \deg \sin(\omega t)$. a) DES results at $\alpha = 22_u$ deg; b) DES results at $\alpha = 16_d$ deg; c) RANS results at $\alpha = 22_u$ deg; d) RANS results at $\alpha = 16_d$ deg.

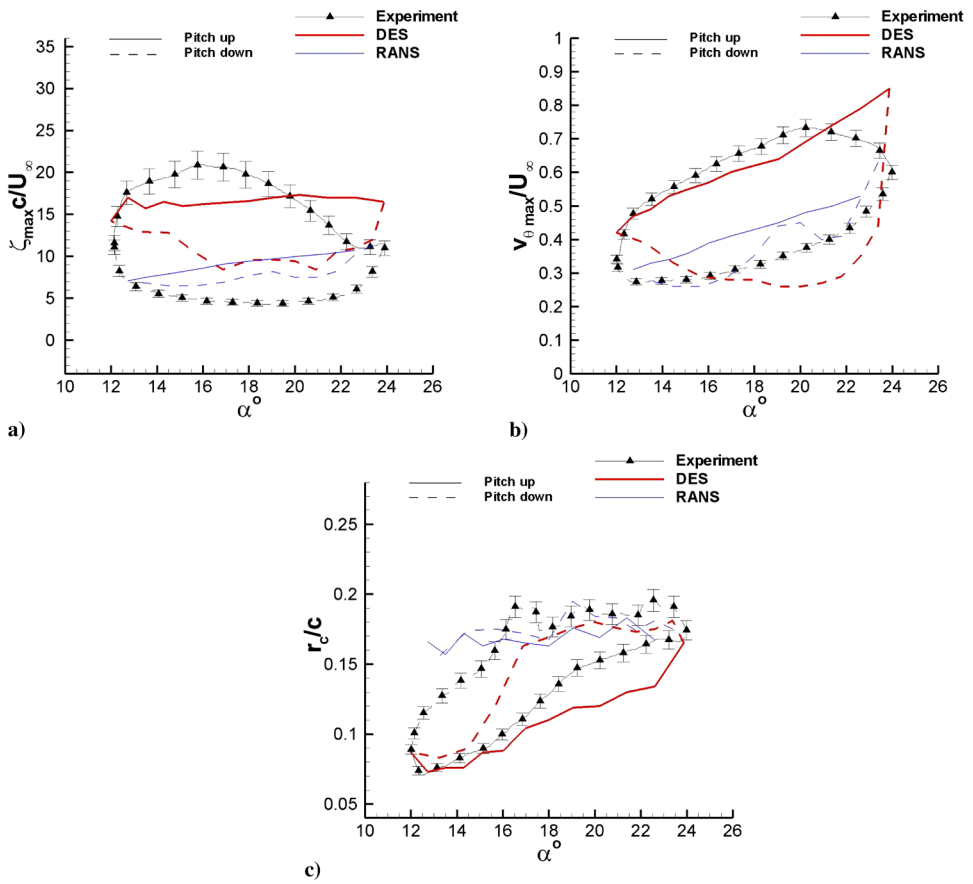

Fig. 14 Variation of vortex parameters with AOA at the $x/c = 1$ plane and comparison with the experimental data [11] for the flow around a NACA0015 wing in pitching oscillations with $\alpha = 18 + 6 \deg \sin(\omega t)$. a) Maximum vorticity; b) maximum tangential velocity; c) core radius.

of attack. In general, DES results revealed better agreement with the experiment in comparison to the RANS simulations where the predicted values at identical AOAs in pitch-up and pitch-down strokes remained almost the same through the whole oscillation cycle, implying a quasi-steady behavior for the downstream evolution of the tip vortex. The dynamic loops were well captured in DES with significantly different values in the pitch-up and pitch-down strokes. At low AOAs, however, in the bottom of the oscillation cycle, DES values in the up- and downstrokes tended to approach each other earlier than what was seen in the experimental data. This is clearly depicted in Fig. 14c, where the difference between the pitch-up and pitch-down values for the vortex core radius at $\alpha < 14$ deg is much smaller than the corresponding experimental data. This behavior is not far from the expectation considering the existence of the fully attached flow at the bottom of the oscillation cycle and the small reduced frequency of 0.09, which together imply a quasi-steady behavior at this region. However, the absence of such a quasi-steady region in the experimental measurements might be due to the existence of some unsteady phenomena such as separated flow regions on the wing upper surface for $\alpha < 14$ deg, which neither was reported in the experimental study nor captured in current numerical simulations. This remains to be thoroughly investigated.

IV. Conclusions

Static and dynamic stalls of a NACA0015 wing and the behavior of its tip vortex at $x/c = 1$ plane were numerically investigated. DES and RANS methodologies were implemented. Maximum vorticity, maximum tangential velocity, and the tip-vortex core radius at $x/c = 1$ plane were numerically calculated and compared with the available experimental data. DES outperformed RANS in predicting the onset of the static stall, flow characteristics over an oscillation cycle, and the tip-vortex configuration at the designated downstream location.

For the stationary wing, DES predictions of various vortex parameters downstream of the wing were far more accurate than those of RANS simulations. For the oscillating wing, RANS failed to capture the unsteady behavior of the tip vortex at the downstream location, whereas the dynamic loops of different tip-vortex parameters were realized by DES. A discrepancy exists between DES results and experimental measurement at the bottom of the oscillation cycle ($\alpha < 14$ deg). This needs to be investigated in future studies.

The main shortcoming of the DES was the computational time; each DES time step was, on average, 3.5 times more expensive than the similar RANS time step. This deficiency will be addressed in future work by implementing an appropriate preconditioning scheme.

References

[1] Spalart, P., Jou, W.-H., Strelets, M., and Allmaras, S., "Comments on the Feasibility of LES for Wings, and on a Hybrid RANS/LES Approach," *Proceedings—First AFOSR International Conference on DNS/LES*, Greyden Press, Columbus, OH, 1997, pp. 137–147.

[2] Squires, K. D., Forsythe, J. R., and Spalart, P. R., "Detached-Eddy Simulation of the Separated Flow Over a Rounded-Corner Square," *Journal of Fluids Engineering*, Vol. 127, No. 5, 2005, pp. 959–966. doi:10.1115/1.1990202

[3] Crippa, S., and Rizzi, A., "Initial Steady/Unsteady CFD Analysis of Vortex Flow Over the VFE-2 Delta Wing," *Proceedings of the 25th International Congress of the Aeronautical Sciences*, ICAS Secretariat, Stockholm, Sweden, 2006.

[4] Morton, S. A., Kholodar, D., Billingsley, T., Forsythe, J. R., Wurtzler, K. E., Squires, K. D., Cummings, R. M., and Spalart, P. R., "Multidisciplinary Applications of Detached-Eddy Simulation to Separated Flows at High Reynolds Numbers," *Proceedings—Department of Defense High Performance Computing Modernization Program Users Group Conference, UGC 2004*, IEEE Computer Society, Los Alamitos, CA, 2004, pp. 103–111.

[5] Barone, M. F., and Roy, C. J., "Evaluation of Detached Eddy Simulation for Turbulent Wake Applications," *AIAA Journal*, Vol. 44, No. 12, 2006, pp. 3062–3071. doi:10.2514/1.22359

[6] Travin, A., Shur, M., Strelets, M., and Spalart, P., "Physical and Numerical Upgrades in the Detached-Eddy Simulation of Complex Turbulent Flows," *Advances in LES of Complex Flows*, Springer, New York, 2002, pp. 239–254.

[7] Bunge, U., Mockett, C., and Thiele, F., "Guidelines for Implementing Detached-Eddy Simulation Using Different Models," *Aerospace Science and Technology*, Vol. 11, No. 5, 2007, pp. 376–385. doi:10.1016/j.ast.2007.02.001

[8] Spalart, P., Deck, S., Shur, M., Squires, K., Strelets, M., and Travin, A., "A New Version of Detached-Eddy Simulation, Resistant to Ambiguous Grid Densities," *Theoretical and Computational Fluid Dynamics*, Vol. 20, No. 3, 2006, pp. 181–195. doi:10.1007/s00162-006-0015-0

[9] Freymuth, P., Bank, W., and Finaish, F., "Visualization of Wing Tip Vortices in Accelerating and Steady Flow," *Journal of Aircraft*, Vol. 23, No. 9, 1986, pp. 731–733.

[10] Chang, J. W., and Park, S. O., "Measurements in the Tip Vortex Roll-Up Region of an Oscillating Wing," *AIAA Journal*, Vol. 38, No. 6, 2000, pp. 1092–1095. doi:10.2514/2.1072

[11] Birch, D., and Lee, T., "Tip Vortex Behind a Wing Undergoing Deep-Stall Oscillation," *AIAA Journal*, Vol. 43, No. 10, 2005, pp. 2081–2092. doi:10.2514/1.13139

[12] Birch, D., and Lee, T., "Investigation of the Near-Field Tip Vortex Behind an Oscillating Wing," *Journal of Fluid Mechanics*, Vol. 544, 2005, pp. 201–241. doi:10.1017/S0022112005006804

[13] Ekaterinaris, J. A., and Platzer, M. F., "Computational Prediction of Airfoil Dynamic Stall," *Progress in Aerospace Sciences*, Vol. 33, Nos. 11–12, 1997, pp. 759–846.

[14] Newsome, R., "Navier-Stokes Simulation of Wing Tip and Wing Juncture Interactions for a Pitching Wing," AIAA Paper 94-2259, 1994.

[15] Szydlowski, J., and Costes, M., "Simulation of Flow Around a NACA0015 Airfoil for Static and Dynamic Stall Configurations Using RANS and DES," *AHS International 4th Decennial Specialists' Conference on Aeromechanics*, American Helicopter Society, Alexandria, VA, 2004, pp. 223–238.

[16] Spentzos, A., Barakos, G., Badcock, K., Richards, B., Coton, F., Galbraith, R. A. M., Berton, E., and Favier, D., "Computational Fluid Dynamics Study of Three-Dimensional Dynamic Stall of Various Planform Shapes," *Journal of Aircraft*, Vol. 44, No. 4, 2007, pp. 1118–1128. doi:10.2514/1.24331

[17] Spalart, P., and Allmaras, S., "One-Equation Turbulence Model for Aerodynamic Flows," *Recherche Aerospatiale*, No. 1, 1994, pp. 5–21.

[18] Donea, J., Giuliani, S., and Halleux, J. P., "Arbitrary Lagrangian-Eulerian Finite Element Method for Transient Dynamic Fluid-Structure Interactions," *Computer Methods in Applied Mechanics and Engineering*, Vol. 33, Nos. 1–3, 1982, pp. 689–723. doi:10.1016/0045-7825(82)90128-1

[19] Hallo, L., Le Ribault, C., and Buffat, M., "Implicit Mixed Finite-Volume-Finite-Element Method for Solving 3D Turbulent Compressible Flows," *International Journal for Numerical Methods in Fluids*, Vol. 25, No. 11, 1997, pp. 1241–1261. doi:10.1002/(SICI)1097-0363(19971215)25:11<1241::AID-FLD595>3.0.CO;2-1

[20] Lesoinne, M., and Farhat, C., "Geometric Conservation Laws for Flow Problems with Moving Boundaries and Deformable Meshes, and Their Impact on Aeroelastic Computations," *Computer Methods in Applied Mechanics and Engineering*, Vol. 134, Nos. 1–2, 1996, pp. 71–90. doi:10.1016/0045-7825(96)01028-6

[21] Farhat, C., Lesoinne, M., and Stern, P., "High Performance Solution of Three-Dimensional Nonlinear Aeroelastic Problems via Parallel Partitioned Algorithms: Methodology and Preliminary Results," *Advances in Engineering Software*, Vol. 28, No. 1, 1997, pp. 43–61. doi:10.1016/S0965-9978(96)00028-2

[22] Nkonga, R., and Guillard, H., "Godunov Type Method on Non-Structural Meshes for Three-Dimensional Moving Boundary Problems," *Computer Methods in Applied Mechanics and Engineering*, Vol. 113, Nos. 1–2, 1994, pp. 183–204. doi:10.1016/0045-7825(94)90218-6

[23] Sarkis, M., and Koobus, B., "A Scaled and Minimum Overlap Restricted Additive Schwarz Method with Application to Aerodynamics," *Computer Methods in Applied Mechanics and Engineering*, Vol. 184, Nos. 2–4, 2000, pp. 391–400. doi:10.1016/S0045-7825(99)00236-4

[24] Saad, Y., *Iterative Methods for Sparse Linear Systems*, 2nd ed., Society for Industrial and Applied Mathematics (SIAM), Philadelphia, PA, 2003.

[25] Turkel, E., and Vatsa, V., "Local Preconditioners for Steady and

Unsteady Flow Applications," *Mathematical Modelling and Numerical Analysis*, Vol. 39, No. 3, 2005, pp. 515–35.

[26] Viozat, C., "Implicit Upwind Schemes for Low Mach Number Compressible Flows," Rapport, Institute National de Recherche en Informatique et en Automatique, INRIA, Rept. 3084, Jan. 1997.

[27] Jeong, J., and Hussain, F., "On the Identification of a Vortex," *Journal of Fluid Mechanics*, Vol. 285, 1995, pp. 69–94. doi:10.1017/S0022112095000462

[28] Spalart, P., "Young-Person's Guide to Detached-Eddy Simulation Grids," NASA TR CR-2001-211032, 2001.

[29] Karypis, G., and Kumar, V., "A Software Package for Partitioning Unstructured Graphs, Partitioning Meshes, and Computing Fill-Reducing Ordering of Sparse Matrices," TR, University of Minnesota, Department of Computer Science/Army HPC Research Center, 1998.